



Laminar transpiration cooling experiments in hypersonic flow

Hassan Saad Ifti¹ · Tobias Hermann¹ · Marc Ewenz Rocher¹ · Luke Doherty¹ · Christopher Hambidge¹ · Matthew McGilvray¹ · Luc Vandeperre²

Received: 22 November 2021 / Revised: 21 April 2022 / Accepted: 23 April 2022 / Published online: 4 June 2022
© The Author(s) 2022

Abstract

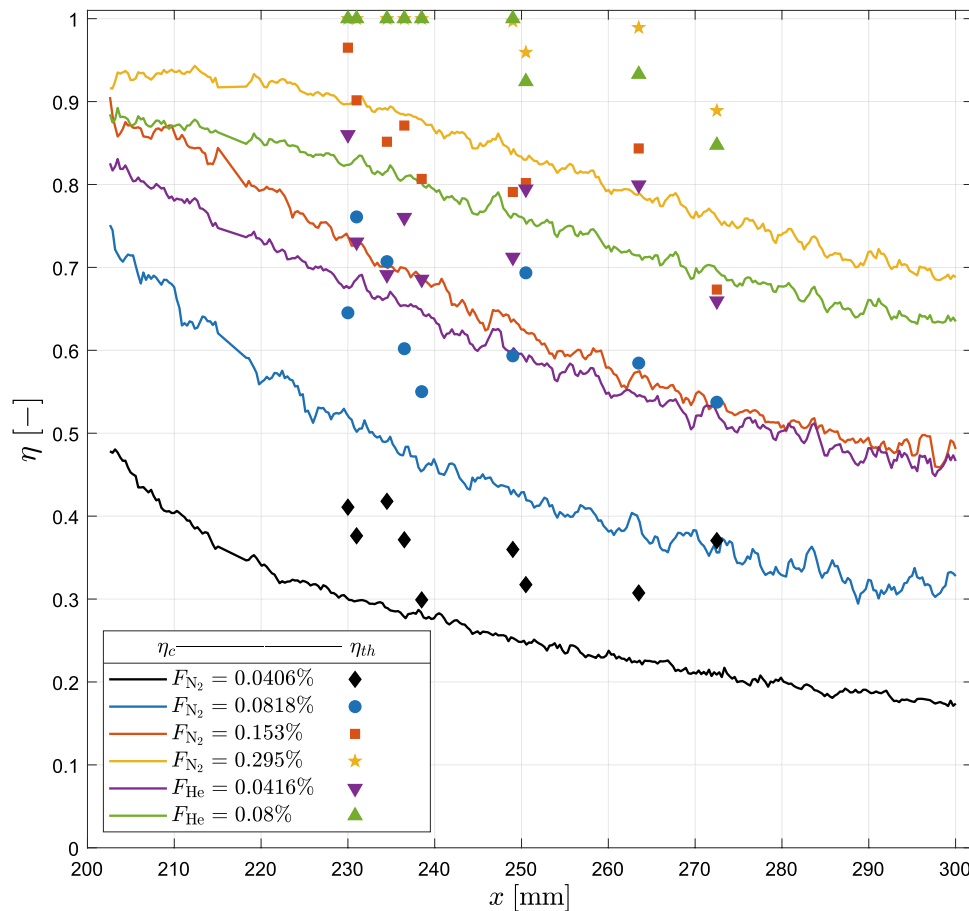
The mixing between the coolant and the boundary-layer gas downstream of an injector—for transpiration/film cooling—has been extensively studied for turbulent flows; however, only a handful of studies concerning laminar mixing exist, particularly in hypersonic flows. In this paper, the concentration of the coolant gas at the wall and the heat flux reduction downstream of a transpiring injector in a hypersonic laminar flow are experimentally measured and examined. Experiments are performed in the Oxford High Density Tunnel at Mach 7. A flat-plate model is coated with pressure-sensitive paint (PSP) to spatially resolve the film and obtain a film effectiveness based on coolant concentration. Thin-film arrays are installed to measure the heat flux reduction. Six different cases are studied featuring nitrogen and helium as the coolant gas, where the blowing ratio is varied from 0.0406% to 0.295%. The unit Reynolds number of the flow is $12.9 \times 10^6 \text{ m}^{-1}$. A coolant concentration of up to 95% is achieved immediately (2 mm) downstream of the injector. The film concentration drops in a monotonic fashion farther downstream; however, a constant film coverage of 5–20 mm immediately downstream of the injector is observed in cases with a higher blowing ratio. A film coverage above 15% over three injector lengths is present even for the lowest blowing ratio. Heat flux reduction is achieved in all cases. The concentration effectiveness obtained from PSP is compared with the thermal film effectiveness calculated from the heat flux reduction. The latter is found to be higher than the former for all data points. Finally, a collapse of the thermal effectiveness is achieved and a modified analytical correlation is proposed.

✉ Hassan Saad Ifti
saad.ifti@eng.ox.ac.uk

¹ Department of Engineering Science, Hypersonics Group,
Oxford Thermofluids Institute, University of Oxford,
Oxford, OX2 0ES, UK

² Department of Materials, Imperial College London, Royal
School of Mines, Exhibition Road, London SW7 2AZ, UK

Graphical abstract



1 Introduction

Hypersonic vehicles are subject to extremely high heat fluxes due to aerodynamic heating (van Driest 1956), which becomes detrimental for the vehicle at very high Mach numbers. Different types of Thermal Protection Systems (TPS) are therefore in use today that protect the vehicles from overheating. Although these state-of-the-art heat mitigation techniques—such as heat sinks (passive) and ablation (semi-passive)—are successful for vehicles operated at present, these conventional thermal protection systems often have a low degree of re-usability, especially when the vehicle experiences high peak heating. This constraint results in a higher cost of payload transfer. A re-usable, high-performing thermal protection system could therefore drive this cost down, making space and hypersonic flight more accessible. The pursuit of a novel, re-usable TPS is critical to both present and future hypersonic flight. Transpiration cooling is a promising, candidate technology that

could enable a re-usable TPS for hypersonic vehicles such as rockets or spaceplanes. In particular, it could be employed in conjunction with conventional thermal protection systems for vehicle parts that experience high peak heating such as leading edges or control-fin joints (e.g. the joint between the fuselage and a stabiliser or canard). Transpiration cooling is an active cooling method where a coolant gas is injected through a porous material into the boundary-layer. The cooling process comprises three different effects (see Fig. 1): (a) heat from the wall is convected out by the fluid; (b) the coolant gas creates a film (blue) that insulates the wall underneath from the hot cross-flow; and (c) the coolant film protects the wall from free-stream Oxygen and thereby prevents oxidation of the wall, which enables the wall material to operate at a higher temperature enhancing radiative cooling and reduces recombination heating. The success of the latter two processes depends on the coolant film that is formed on and downstream of the injector. This protective film loses its concentration in the stream-wise direction and

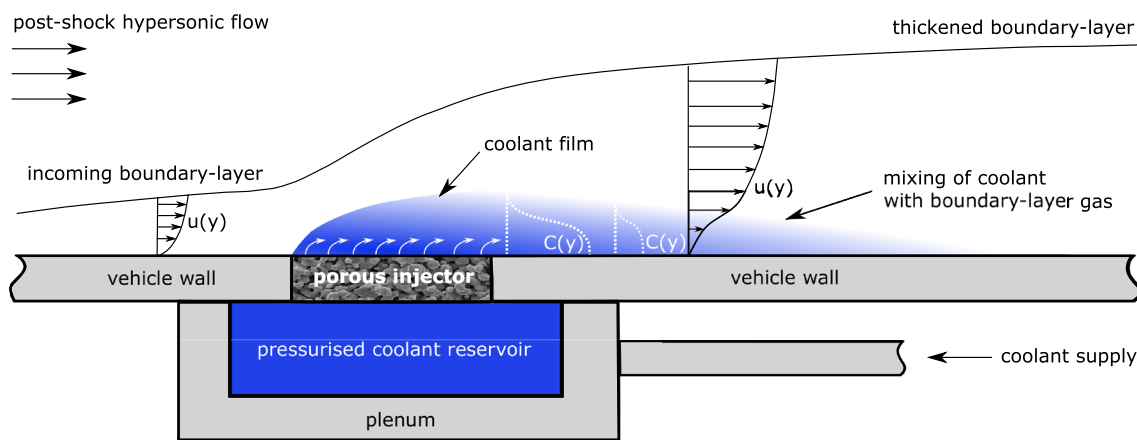


Fig. 1 Schematic of a flat surface of a hypersonic vehicle with a porous, transpiration cooling injector. Note: not to scale

eventually diminishes at a downstream location as it mixes with the incoming hypersonic cross-flow (see the concentration gradient, $C(y)$ in Fig. 1). In practice, transpiration cooling would act as a dual-mode protection system that would protect the vehicle from both heat and oxidation.

For successful application of this technology on a vehicle, it is necessary to first understand the fundamental mechanics of the subprocesses. The majority of the studies in the literature are therefore concerned with a common goal of understanding—and in some cases predicting—the mixing between the coolant gas and the external cross-flow. This mixing problem of transpiration cooling can be divided in two regions: (1) on the porous injector and (2) downstream of the injector. Authors have correlated the blowing ratio of the coolant gas, i.e. the ratio between the coolant mass flux and the free-stream mass flux (Eq. 1), with the cooling effectiveness in various conditions with different gasses. There is a vast amount of work in the literature on this topic spanning more than 50 years (Goldstein 1971; Fujiwara et al. 2017). However, most studies are concerned with turbulent flows only, and there is a need for developing additional experimental techniques to further understand the underlying physics of the problem of mixing in transpiration/film cooling.

A hypersonic vehicle may fly through all three flow regimes, i.e. laminar, transitional, and turbulent, and therefore cooling in each flow regime could become important for such a vehicle. What is more, a hypersonic vehicle could experience its highest peak heating in the laminar regime (Hermann et al. 2019b). Despite this need, only a handful of studies on film cooling or transpiration cooling in a laminar boundary-layer are available in the literature, experimental and numerical studies combined. Heufer and Olivier (2008a) proposed a correlation factor based on the energy equation similar to Goldstein (1971) but with a laminar velocity profile. The authors validated the correlation factor numerically and experimentally using a slot injector on a flat-plate in

laminar, supersonic flows and achieved a collapse of the data. Different slot geometries and coolant gasses were used in the experiments by Hombsch and Olivier (2013) in supersonic flows, where the authors demonstrated that film cooling was much more effective in laminar flows than turbulent ones, and a correlation was proposed. Keller et al. (2015) performed direct numerical simulations to investigate the influence of different coolant gasses in a Mach 2.6, laminar flow over a flat-plate and compared the simulation to the data from Hombsch and Olivier (2013) and demonstrated a collapse of the data for different gasses by multiplying the correlation factor by the ratio of specific heat capacities raised to the exponent of 0.33. The success of film cooling in laminar, hypersonic flows was demonstrated by Heufer and Olivier (2008b) where a flat-plate model was used featuring a slot injector. Gülhan and Braun (2010) further demonstrated the high efficiency of transpiration cooling downstream of a porous injector in laminar, hypersonic flows over a flat-plate. One of the earlier experimental studies was conducted by Richards and Stollery (1979), where tangential injection was employed to cool a flat-plate in a hypersonic boundary-layer at Mach 10. The authors proposed a discrete-layer theory based on heat conduction. All of these studies, however, concern heat flux reduction only, not the concentration of the coolant gas at the wall. Since the heat and mass transfer analogy does not apply to laminar flows (Kays et al. 2005), the coolant gas's concentration distribution on the wall becomes a compelling quantity in order to understand the mixing process in laminar boundary-layers. However, experimental data on the concentration distribution, particularly in laminar, hypersonic flows, are not available in the literature.

In this paper, the concentration of the transpiring coolant gas at the wall downstream of the injector—along with the corresponding heat flux reduction—is experimentally measured and examined in a laminar, hypersonic boundary

layer. This is the first time the distribution of the coolant's concentration at the wall downstream of a transpiring injector in a laminar hypersonic flow is reported. A flat-plate model is used in the Oxford High Density Tunnel (HDT) at Mach 7. This model allows to investigate the mixing problem without any geometric complexity and contributes to the existing, large body of work in the literature based on flat-plate geometries (e.g. Heufer and Olivier 2008a; Hombsch and Olivier 2013; Hermann et al. 2019b; Gülhan and Braun 2010). A porous injector made of partially sintered zirconium diboride (ZrB_2) is used (diameter of its pores is below $10\ \mu\text{m}$). The coolant film concentration at the wall downstream of the injector is spatially resolved using Pressure-sensitive Paint (PSP). The corresponding heat flux reduction is measured with thin-film gauges.

2 Methodology

The experiments were conducted in the Oxford High Density Tunnel (HDT) that was operated in Ludwig tube mode (McGilvray et al. 2015; Wylie and McGilvray 2019; Wylie 2020) at Mach 7. Data were acquired on an NI PXIe-8135 controller with NI PXIe-6368 acquisition cards at 2 MS/s/channel. A flat-plate model was employed that was mounted at an angle of attack of $\text{AoA} = 0^\circ$. For reference, the core flow diameter ranges from 280 to 320 mm at the nozzle exit and from 200 to 240 mm at an axial location 418 mm downstream thereof (Wylie 2020). The experimental model and diagnostic methods are discussed in Sects. 2.1, 2.2, 2.3, and 2.4.

2.1 Flat-plate model

A flat-plate model with a top surface area of $577\ \text{mm} \times 125\ \text{mm}$ was employed (see Fig. 2a). The top plates were made of C250 tooling plates (roughness R_a of 0.4 microns). The joints between the plates were made flush by centring dowel pins and any gap between the joints was filled with cement to ensure a smooth finish. A porous injector (made of ZrB_2) of $39.5\ \text{mm} \times 39.5\ \text{mm}$ was placed on the symmetry line of the plate at $x = 160\ \text{mm}$ from the leading edge (see Fig. 2b for microstructure). A plenum was attached underneath the porous injector and pipework was in place to feed in the injection gas. The plenum was fitted with a thin ($\phi 0.0762\ \text{mm}$), fast-response K-type thermocouple (in-house, response time $< 1\ \text{ms}$) and a Kulite pressure transducer (HEL-375-35BARA) in order to measure the temperature and pressure of the coolant gas, respectively. The model featured a coat of the porous, fast-response pressure-sensitive paint (PSP) (Sellers et al. 2016) from Innovative Scientific Solutions, Inc. (ISSI) on the surface downstream of the porous injector—starting at $x = 200\ \text{mm}$ from the leading edge—on one side of the symmetry line. This is a three-component, single-luminophore PSP that has a response time under $100\ \mu\text{s}$, a pressure sensitivity of 0.6% per kPa, and a range of 0–200 kPa. The PSP coat had an area of interrogation of $140\ \text{mm} \times 37\ \text{mm}$. On the other side of the symmetry line, Macor-based platinum thin-film arrays were instrumented upstream (6 active gauges from $x = 96\ \text{mm}$ to $116\ \text{mm}$) and downstream (16 active gauges from $x = 230\ \text{mm}$ to $358\ \text{mm}$) of the injector. The plate was further instrumented with four flush-mounted Kulite pressure transducers (XCS-093-5A) at locations $x = 46\ \text{mm}$,

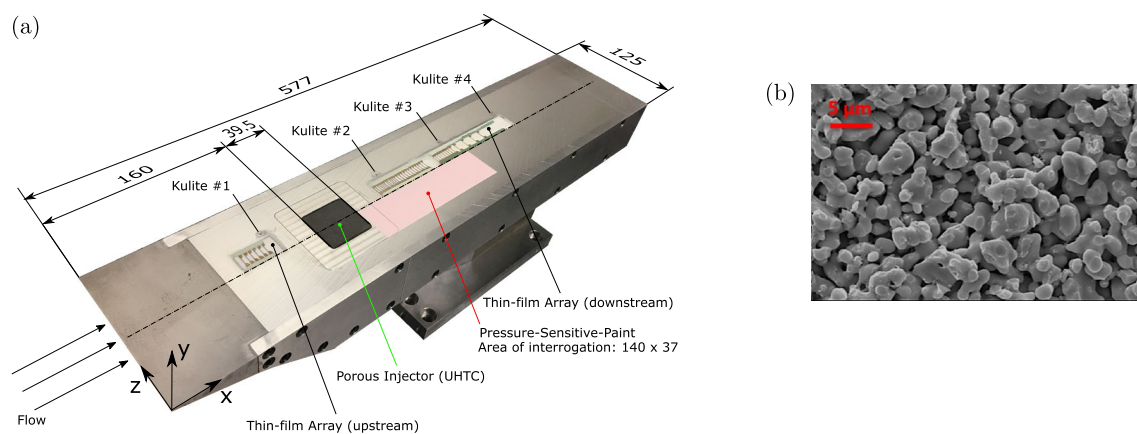


Fig. 2 **a** Flat-plate model instrumented with Kulite pressure transducers, thin-film arrays, and a porous injector (UHTC). A PSP layer is painted downstream of the injector. Note: all dimensions are in mil-

limetres. **b** A scanning electron microscopy (SEM) micrograph of the microstructure of the UHTC injector (Ifti et al. 2022)

Table 1 Overview of blowing cases. Flow condition: $Re_u = 12.9 \times 10^6 \text{ m}^{-1}$, $p_0 = 1.738 \text{ MPa}$, and $T_0 = 470.1 \text{ K}$. Uncertainties in F and B_h are, respectively, $\pm 11.0\%$ and $\pm 29.5\%$

Case	F [%]	B_h [-]	Coolant gas
1	0.0406	1.49	N_2
2	0.0818	2.99	N_2
3	0.153	5.59	N_2
4	0.295	10.8	N_2
5	0.0416	1.52	He
6	0.08	2.93	He

$x = 168 \text{ mm}$, $x = 250 \text{ mm}$, and $x = 332 \text{ mm}$. In addition to measuring heat flux, the thin-film arrays were employed to determine the boundary-layer state, i.e. laminar, transitional, or turbulent, with no injection.

2.2 Flow condition and blowing ratios

The blowing ratio, i.e. the ratio of the injected coolant mass flux to the boundary-layer edge mass flux, is defined as

$$F = \frac{\rho_c u_c}{\rho_e u_e}, \quad (1)$$

where the subscripts ‘c’ and ‘e’, respectively, denote coolant quantities at the surface and the edge quantities. ρ and u are density and velocity, respectively. The blowing parameter, on the other hand, is given by the equation

$$B_h = \frac{F}{St_0}, \quad (2)$$

where St_0 is the Stanton number on the injector at $F = 0$. In Table 1, the six blowing ratios used in this study are presented along with their respective blowing parameters. Nitrogen was used as the coolant gas for Cases 1 to 4 and helium for Cases 5 to 6. The Mach number, unit Reynolds number, total pressure, and total temperature were, respectively, $M = 7$, $Re_u = 12.9 \times 10^6 \text{ m}^{-1}$, $p_0 = 1.738 \text{ MPa}$, and $T_0 = 470.1 \text{ K}$. Further details on the calculation of flow quantities are presented in “Appendix 1” and an uncertainty analysis for relevant quantities are given in “Appendix 3”.

The outflow distribution of the employed porous injector was characterised by hot-wire anemometry with air injection. Details of the process can be found in Ifti et al. (2022). The obtained velocity map is illustrated in Fig. 3.

2.3 Measurement of wall coolant concentration

The relative coolant concentration on the wall was measured by pressure-sensitive-paint (PSP). A Luminus PT-120-TE UV high-power LED was positioned above the model. The

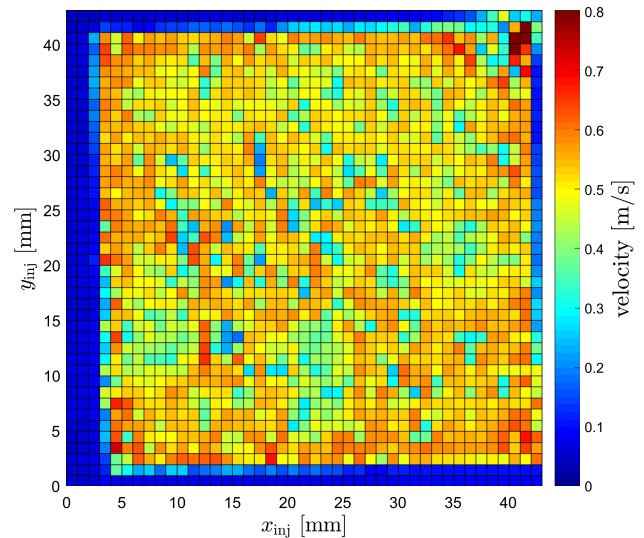


Fig. 3 Velocity map of the porous ZrB_2 injector. Injected gas: air. Gas temperature: $24 \text{ }^\circ\text{C}$. Differential pressure: 4 bar. Thickness of injector: 5 mm

LED was turned on for approximately 5 s before each shot. The LED temperature rises when it is operated, which was measured by its built-in thermistor. The LED intensity is a linear function of its temperature, and therefore the recorded intensity was scaled by the measured LED temperature rise to allow for repeatable illumination between shots. The emitted radiation passed through a UV bandpass filter with a central wavelength of 390 nm and a full width at half maximum of 125 nm. The luminophore in the porous fast-response pressure-sensitive paint is excited by the UV radiation and achieves a higher state of energy that results in an emission in the red wavelength spectrum as it returns to its ground state. The emitted radiation from the PSP reflected off a flat mirror and was captured by a high-speed camera (Photron FASTCAM Mini AX200 type 900K) that was fitted with a red filter (550 nm) and placed outside the test section (Hermann et al. 2018). The images were captured at a frame rate of 6400 fps, shutter speed of $156.25 \mu\text{s}$, a bit depth of 12, and a resolution of 1024×512 . The acquisition of images was started before the flow arrival and continued for the whole duration of the test. The images were spatially transformed to a rectangle that represents the physical geometry of the flat-plate model and passed through an image stabilisation algorithm prior to post-processing. A schematic of the PSP setup is illustrated in Fig. 4.

The excitation of PSP luminophores is quenched by oxygen, and therefore, an increase in oxygen partial pressure, p_{O_2} , results in a lower intensity, I , of the emitted radiation, and vice versa. This characteristic can be expressed in the power law form of the Stern–Volmer equation (Quinn et al. 2011) as

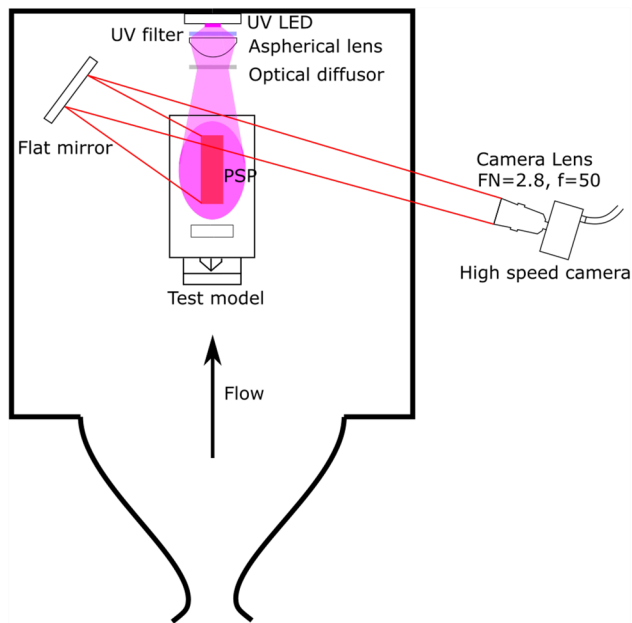


Fig. 4 Schematic of the PSP setup (not to scale). Figure from Hermann et al. (2018)

$$\frac{I_{\text{ref}}}{I} = c_1 p_{O_2}^n + c_2, \quad 0 < n \leq 1.0. \quad (3)$$

Here, I_{ref} refers to the intensity reference value taken before the flow arrival. The coefficients, c_1 , c_2 , and n were determined by a regression analysis from calibration data. For the current experiments, the reference value were taken prior to the flow arrival when the test section was near vacuum (approximately 80 Pa). A pixel-by-pixel calibration was performed by collecting data from a shot without injecting any coolant gas. The pressure values were obtained from the average pressure measured by the surface-mounted Kulites. Five data points are obtained from five different flow conditions for pressure, p_{O_2} , and intensity ratio, I_{ref}/I , and an additional data point is obtained from the data acquired prior to the flow arrival. Calibration data were collected on a daily basis to reduce the effect of PSP degradation. The R-squared value (coefficient of determination) for each pixel was calculated to quantify the quality of regression. The spatially averaged (across all pixels) R-squared value for these calibrations is $R^2 \geq 0.99$. Since the same calibration is applied to all the other shots with gas injection, a trace of the film can be identified as the quenching is influenced by the film. Injected nitrogen or helium gas hinders the quenching by displacing air in the boundary-layer. Comparing a case with air injection and one with a foreign gas injection at the same blowing ratio, in this case nitrogen or helium, gives a measure of how much air is displaced by the foreign gas, i.e. to what extent the foreign gas is forming a film. A concentration film effectiveness is defined as

$$\begin{aligned} \eta_c &= \frac{C_w - C_e}{C_c - C_e} \\ &= 1 - \frac{p_{O_2, \text{foreign gas}}}{p_{O_2, \text{air}}}, \end{aligned} \quad (4)$$

where C is the concentration and subscript ‘w’ stands for concentration at the wall; $p_{O_2, \text{air}}$ and $p_{O_2, \text{foreign gas}}$ are oxygen partial pressures with air and foreign gas injections, respectively, at the same blowing ratio. A concentration film effectiveness of $\eta_c = 1$ corresponds to a full displacement of the air by the foreign gas, whereas $\eta_c = 0$ indicates that no displacement of air is achieved and the film is fully diminished. Since η_c is calculated for every pixel, it yields a spatial map of the whole film downstream of the porous injector. Essentially, this film effectiveness based on coolant concentration quantifies the physical presence of the film in terms of its concentration. Unlike in the case of turbulent flow, this effectiveness is not equivalent to the thermal effectiveness as the heat and mass transfer analogy cannot be assumed in laminar flows. Equation (4) is strictly a measure of relative concentration.

2.4 Heat flux measurement and determination of boundary-layer state

The thin-film arrays measure the heat flux along the stream-wise direction. As the flow convects over the plate, the temperature of the Macor rises. This recorded temperature rise, ΔT , is used to compute the wall heat flux, \dot{q}_w , by applying the impulse response convolution approach of Oldfield (2008). The thermal product of Macor is $\sqrt{\rho c_p k} = 1705 \text{ Jm}^{-2}\text{K}^{-1}\text{s}^{-0.5}$ (Macor data sheet). The impulse response is calculated with an assumption of heat conduction into a one-dimensional semi-infinite slab. According to Schultz and Jones (1973), this assumption is valid as long as the thermal penetration depth during the test is shorter than the thickness of the material. For Macor, this minimum depth is 2.65 mm over a time period of 600 ms. The Macor arrays installed in the flat-plate had a minimum depth of 7 mm.

The heat flux measurement had two purposes: (a) to quantify the heat flux reduction by transpiration cooling and (b) to determine the boundary-layer state. The latter was achieved by measuring the heat flux without coolant injection and comparing it to Eckert’s heat flux correlations for laminar and turbulent boundary layers over a flat plate (Eckert 1956), respectively, expressed as

$$St_{\text{lam}}^* = \frac{0.332}{\sqrt{Re_x^*}} (Pr^*)^{-2/3} \quad (5)$$

and

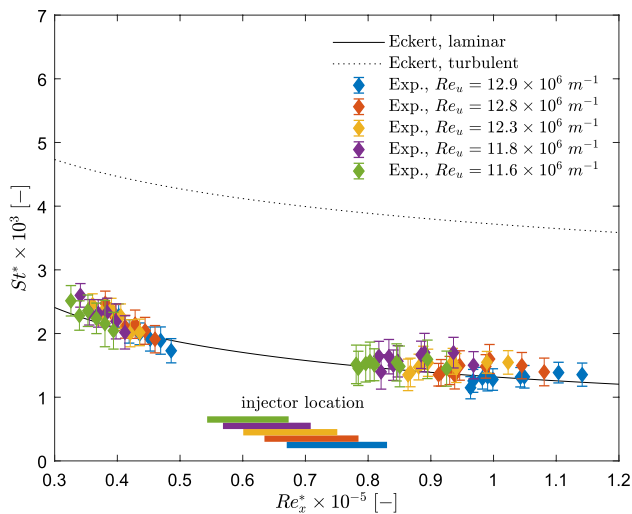


Fig. 5 Comparison with Eckert correlation: St^* versus Re_x^* at $F = 0$

$$St_{turb}^* = \frac{0.0296}{(Re_x^*)^{0.2}} (Pr^*)^{-2/3}. \tag{6}$$

Here, St is the Stanton number. The superscript ‘*’ here denotes quantities that are evaluated at Eckert’s reference temperature.

In Fig. 5, the experimentally obtained heat flux data for five different flow conditions—from a shot without coolant injection—are plotted versus Re_x^* . The Eckert reference curves for laminar and turbulent boundary layers, i.e. Eqs. (5) and (6), are illustrated alongside. The experimental data points lie atop Eckert’s laminar curve upstream (all 6 active gauges shown) of the injector as well as immediately downstream (all active gauges up to 272.5 mm shown). The onset of natural transition (no blowing) took place approximately at $x = 310$ mm (not shown in Fig. 5).

The heat flux reduction by transpiration cooling is formulated as the isothermal cooling effectiveness

$$\eta_{th} = 1 - \frac{St_c}{St_0}, \tag{7}$$

where the subscripts ‘c’ and ‘0’, respectively, denote cooled and uncooled cases. A case of 100% cooling, i.e. zero heat flux to the wall, would result in an effectiveness of 1. Eq. (7) is only valid for small blowing ratios and cases where the coolant gas is similar to the free-stream gas (Heufer and Olivier 2008a). It is also invalid for downstream locations that are close to the injector. The obtained values of η_{th} can be correlated by a factor defined by Heufer and Olivier (2008a) as

$$\xi = \frac{1}{Fs} \sqrt{\frac{x - x_s}{x_s^{1.16}} \frac{C^* x}{Re_u}}, \tag{8}$$

where x_s is the slot location from the leading edge, s is the slot length, and C^* is the Chapman–Rubesin factor evaluated at Eckert’s reference temperature. The effect of different coolant gases can be taken into account by multiplying the correlation factor, ξ , by the ratio of the specific heat capacities of the free-stream gas and the coolant gas, $c_{p,e}/c_{p,c}$, with an appropriate exponent, which has been demonstrated by Keller et al. (2015). Hombsch and Olivier (2013) proposed the correlation obtained from experimental data for blowing ratios ranging from 2.2% to 10.7% expressed as

$$\eta_{th} = \begin{cases} 1 & \text{for } \xi \leq 0.96, \\ [1 + 0.38(\xi - 0.96)]^{-1.6} & \text{for } \xi > 0.96. \end{cases} \tag{9}$$

3 Results and discussion

Contour plots of oxygen partial pressure, p_{O_2} , are presented in Fig. 6a–f for all blowing cases (see Table 1). Figures of the corresponding concentration effectiveness, η_c (obtained from Eq. 4), are, respectively, illustrated in Fig. 6g–l. The origin of the x and y axes is shown in Fig. 2. These contour plots show the physical trace of the film that is spatially resolved. As blowing ratio, F , increases for a given coolant gas, the oxygen partial pressure decreases (Cases 1–4 for nitrogen and Cases 5–6 for helium). This is expected as the injected gas forms a film downstream and displaces the air in the boundary layer, and this process is more successful with higher mass flux of the coolant gas. The plots of concentration effectiveness, on the other hand, visualise the film in terms of the relative concentration of the coolant gas. As expected, the coolant concentration is higher immediately downstream of the injector and gradually reduces downstream with higher values of x . The cases with the highest blowing ratio for nitrogen and helium, i.e. Case 4 and Case 6, respectively, exhibit a concentration effectiveness of approximately 1 ($\eta_c \approx 0.95$) immediately downstream of the injector ($x = 200$ mm to $x = 240$ mm). This indicates that the air is almost fully displaced here and a coolant coverage close to 100% is achieved at this location. With rising blowing ratio, the ‘V’ shape of the film becomes more prominent, which is consistent with the results shown in Hermann et al. (2018). This is due to the Mach angle effect emanating from the two corners of the model as shown in Fig. 12. A two-dimensional (2D) flow can only be assumed within this ‘V’ shaped zone (see ‘‘Appendix 4’’) due to the aspect ratio of the model. In contrast to the non-uniform film coverage discussed in Ifti et al. (2019), the film trace in the current results does not demonstrate noticeable non-uniformities.

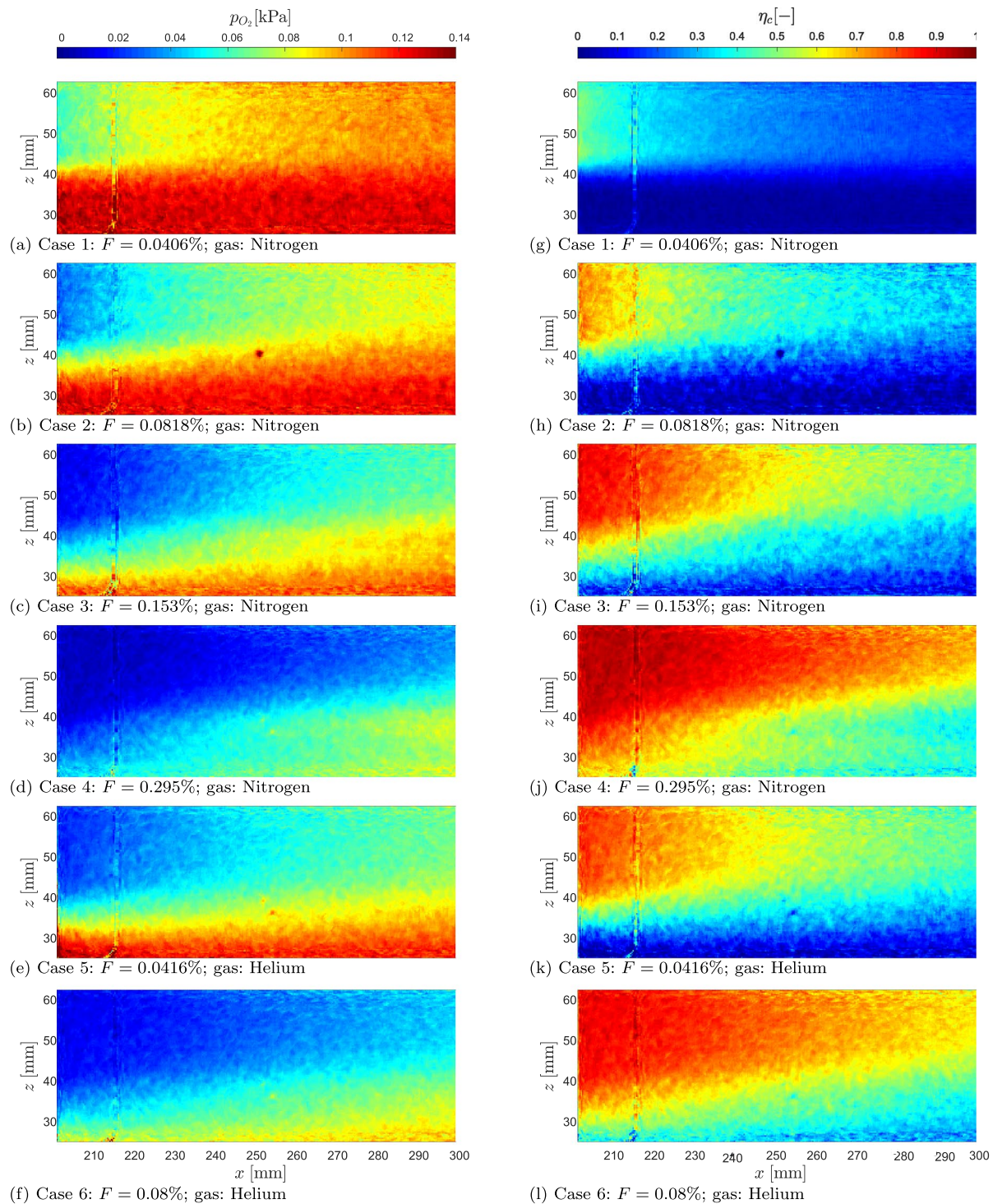


Fig. 6 PSP results for Cases 1 to 6 (top to bottom) at $Re_u = 12.9 \times 10^6 \text{ m}^{-1}$: Contours of downstream oxygen partial pressure, p_{O_2} , from (a) to (f) and film effectiveness, η_c , from (g) to (l).

This is expected because the injector (UHTC-7, see Fig. 3) employed in the current experiments has a significantly more uniform (Ifti et al. 2022, standard deviation of 25.1%, see) outflow than the one used in Ifti et al. (2019).

Refer to Fig. 2a for axis origin. Plots start from $x = 202 \text{ mm}$ on the left. The discontinuity at $x \approx 217 \text{ mm}$ is the joint between the model and the plate that holds the injector (Fig. 2)

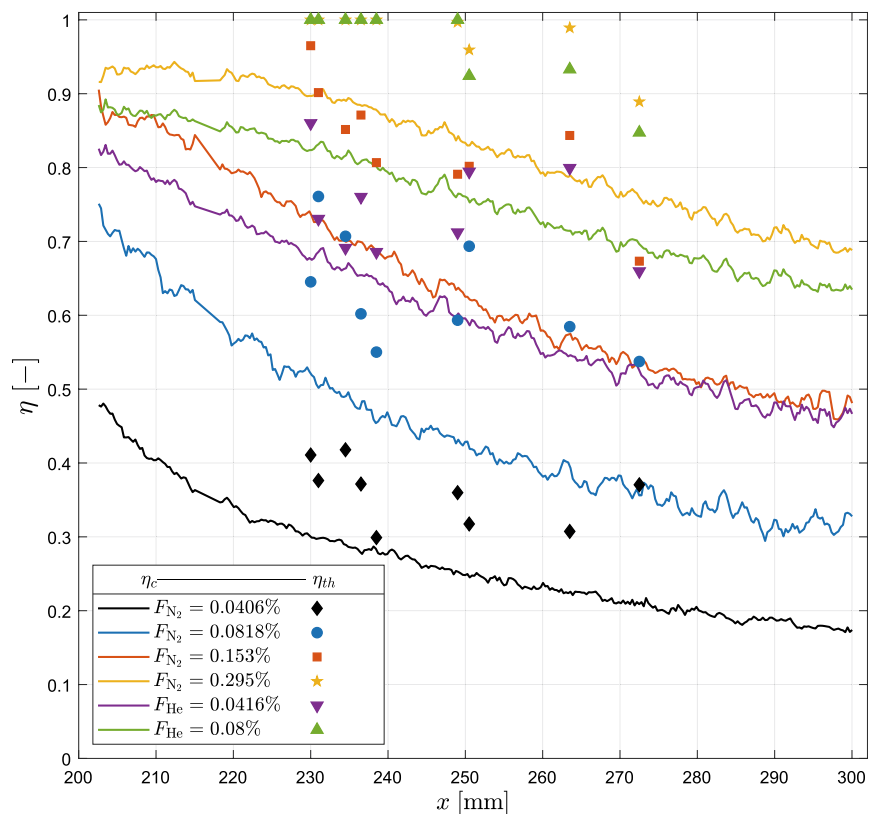
The difference between nitrogen and helium injection can be seen by comparing Cases 1 and 2 (Fig. 6g, h) to Cases 5 and 6 (Fig. 6k, l), respectively. The blowing ratios are matched approximately between Cases 1 and 5 as well as

Cases 2 and 6. A clear difference between the two gases is observed. For approximately the same blowing ratio, the cases with helium injection forms a much stronger film downstream of the injector. This is consistent with the findings reported in the literature, e.g. Richards and Stollery (1979), where helium was shown to be more effective in terms of the heat flux reduction versus nitrogen. However, the results in this paper demonstrate that this is not only due to the gas’s thermal properties but also the physical trace of the film itself. This effect can be attributed to the higher plenum pressure, p_{inj} , required for helium injection compared to nitrogen for the same blowing ratio. Since helium’s molecular weight is lower than that of nitrogen, a higher plenum pressure is required to achieve the same mass flux through the injector. This leads to two differences at the exit: helium exits at a higher velocity due to its lower density at a given edge pressure, p_e , and helium contains more gas particles than nitrogen since a higher plenum pressure results in a higher mole number; in other words, the higher mole number would lead to a larger volume for helium at the exit. Combined, these two effects result in a seven times higher volumetric flow rate, \dot{Q} , of helium when its mass flow rate, \dot{m} , is matched with nitrogen. This higher volumetric flow rate of helium compared to nitrogen accounts for the better film coverage of helium, which has been noted by Gülhan and Braun (2010) and Hombsch and Olivier (2013) as well.

In the case with the highest blowing ratio for either gas, i.e. Case 4 and Case 6, the coolant likely diffuses laterally and therefore the film is wider than the span of the injector (injector edge is at $z = 40$ mm). This effect could also be due to the detachment of the boundary-layer over the injector at these high blowing ratios (Murray et al. 2017) and the resulting kidney vortices at the span-wise edges of the injector (Haven and Kurosaka 1997).

The span-wise averaged values of the concentration effectiveness are plotted versus the stream-wise direction, x , in Fig. 7 (solid lines). The average is taken between $z = 50$ mm and $z = 60$ mm (2.5 mm short of the centreline to avoid noise at the edge resulting from the image stabilisation) assuming a two-dimensional film. As seen in Fig. 6, this assumption is valid all the way up to $x = 300$ mm. The blowing ratio is increased by a factor of 2 (approximately) between the cases for a particular gas (see Table 1). In addition to the absolute values of the concentration effectiveness, a clear discrepancy is noticeable in the shape of the η_c profile. Cases 1 and 2 exhibit a traditional, concave downward, monotonic fall with larger x values, whereas the curves in Cases 3 and 4 start as a plateau downstream of the injector at $x = 200$ mm, drop 10 mm to 20 mm downstream, and follow a concave downward trend after an inflection. The plateaus in Cases 3 and 4 are close to $\eta_c = 0.9$, i.e. almost a full coverage of the coolant gas exists immediately downstream of the injector for these

Fig. 7 a Span-wise averaged concentration effectiveness, η_c (solid line), and thermal effectiveness, η_{th} (marker), versus stream-wise direction, x



relatively higher blowing ratios. The plateau itself indicates a discrete region, where the coolant gas and the boundary-layer gas are still separate. The curves follow a downward trend as the two gas layers start to mix with each other. In contrast, Cases 1 and 2—the cases with the lowest blowing ratios—do not exhibit this discrete region and the start is at $\eta_c \approx 0.5$ and $\eta_c \approx 0.75$ downstream of the injector, which indicates that the mixing already started upstream on the injector. Essentially, with increasing blowing ratio, i.e. coolant mass flux, the film coverage improves on the injector as well as downstream thereof (Cases 1 to 4). With enough coolant mass flux (Cases 3 and 4), a discrete layer is achieved. The coverage of this discrete layer is also dependant on the blowing ratio (Case 3 versus Case 4). As already shown in the contour plots in Fig. 6, the cases with helium injection (Cases 5 and 6) feature a better film coverage than their nitrogen counterparts (Cases 1 and 2), which is visible in Fig. 7 as well. The trend of the curves for Cases 5 and 6 is slightly dissimilar to those of Cases 1 and 2 due to the higher volume and the different form factor of the helium film. The discrete region is not present in Cases 5 and 6; however, Case 6 features a slope immediately downstream of the injector that is close to a plateau. This trend indicates that a discrete region can be formed similar to the nitrogen cases, i.e. Cases 3 and 4, with helium too if the blowing ratio is higher. Overall, a remarkable film coverage above 15% can be achieved up to three injector lengths (3×39.5 mm) downstream of the injector with these relatively low blowing ratios. For reference, a shot-to-shot repeatability of the concentration effectiveness is given in “Appendix 2”.

Figure 7 also shows the thermal effectiveness, η_{th} , for all cases. For the cases with the highest blowing ratio for either gas, i.e. Case 4 and Case 6, the thermal effectiveness is above one at locations nearer to the injector. This is due to negative heat flux at those locations for these cases. The thermal effectiveness is the isothermal cooling effectiveness according to Eq. (7), and therefore a negative Stanton number with injection, i.e. $St_c < 0$, would lead to an effectiveness value of $\eta_{th} > 1$. Essentially, Eq. (7) is not valid at these particular locations and blowing ratios. This effect of over-cooling close to the injector can be observed in the work by Keller et al. (2015), Heufer and Olivier (2008a, b), and Hombsch and Olivier (2013)—all in supersonic or hypersonic flows. The experimentally obtained isothermal cooling effectiveness reported by Heufer and Olivier (2008a, b) and Hombsch and Olivier (2013) are higher than unity immediately downstream of the slot injector. Simulations performed by Keller et al. (2015) yielded an isothermal cooling effectiveness greater than 1.2 within one slot-length downstream of the slot injector when helium was employed as the coolant gas. In this work, values of η_{th} that are greater than one are assigned a value of unity (see Cases 4 and 6 in Fig. 7). The results for thermal effectiveness show that cooling is achieved for all cases and the blowing ratios used in the current tests did not result in

transpiration heating as reported by Tanno et al. (2016), where higher blowing ratios were used.

It can be further observed in Fig. 7 that the thermal effectiveness, η_{th} , is generally higher than the concentration effectiveness, η_c , and can be larger by up to 0.3. A noticeable scatter is present in the data for the thermal effectiveness; however, the trend of $\eta_{th} > \eta_c$ is consistent for the majority of the data points. This is expected since the flow is laminar and the mixing process is not expedited by turbulent mixing and the heat and mass transfer analogy does not apply. In absence of turbulent mixing, the coolant film is diffused into the boundary-layer gas, which is a slower process than turbulent mixing. Hence, a better thermal effectiveness is achieved.

In Fig. 8, the thermal effectiveness, η_{th} , is plotted versus the correlation factor, ξ . A scaling factor of $(c_{p,e}/c_{p,c})^{0.75}$ is used to account for the helium cases. For the current dataset, an exponent of 0.75 was more successful in collapsing the data than the exponent of 0.33 used by Keller et al. (2015). It can be seen that the data points from Cases 5 and 6 that were assigned a value of 1 fall below $\xi(c_{p,e}/c_{p,c})^{0.75} = 0.96$, where the theoretical value is 1. This demonstrates again that Eq. (7) would not apply to these locations. For the remaining cases, a satisfactory collapse of the data is achieved. However, the trend deviates from the correlation by Hombsch and Olivier (2013), i.e. Eq. (9). This is not surprising as the blowing ratios and flow conditions in Hombsch and Olivier (2013) were different (higher blowing ratios, lower Mach numbers). A modified correlation for the data in this work is proposed as follows:

$$\eta_{th} = \begin{cases} 1 & \text{for } \xi \leq 0.96, \\ [1 + 0.4(\xi - 0.96)]^{-1} & \text{for } \xi > 0.96. \end{cases} \quad (10)$$

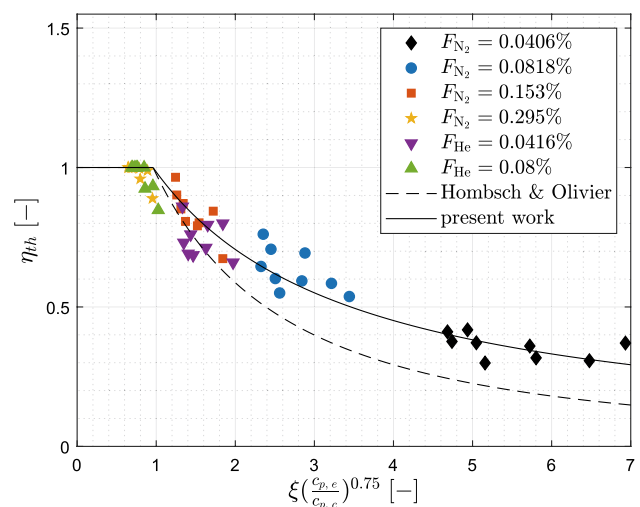


Fig. 8 Thermal effectiveness, η_{th} , versus correlation factor, ξ , at $Re_u = 12.9 \times 10^6 \text{ m}^{-1}$. Present work represents Eq. (10)

The current set of data further demonstrates the difficulty in achieving a general correlation for this mixing problem in laminar flows as opposed to turbulent flows. Since turbulent mixing does not occur in laminar flows, the mixing process is dominated by diffusion and shear-layer effects.

4 Conclusion

The concentration data obtained from pressure-sensitive paint (PSP) show an excellent film coverage for relatively low blowing ratios reaching up to 95% of coolant concentration immediately downstream of the injector. Even 100 mm downstream of the injector, the coolant concentration was found to be approximately 20% for the lowest blowing ratio of 0.0406% with nitrogen injection and approximately 50% for the lowest blowing ratio of 0.0416% with helium injection. For the highest blowing ratio for nitrogen and helium, i.e. 0.295% and 0.08%, respectively, the coolant concentration was, respectively, 70% and 65%, approximately, 100 mm downstream of the injector. For the same blowing ratio, helium forms a more formidable film compared to nitrogen due to its seven times higher volumetric flow rate. For both gases, the film monotonically decays with downstream distance; however, in cases with relatively higher blowing ratios, the film concentration remains constant immediately downstream of the injector, indicating formation of a discrete layer of binary gas. The film eventually starts to decay monotonically farther downstream. In all six cases, a heat flux reduction is achieved downstream of the injector. For the cases with the highest blowing ratio, both with nitrogen and helium, a negative heat flux was recorded immediately downstream of the injector. The effectiveness based on coolant concentration obtained from PSP and the thermal effectiveness acquired from the thin-film arrays are compared. It is shown that the latter is generally higher than the former. Finally, a collapse of the thermal effectiveness is achieved and a modified correlation is proposed. The results published here add to the insight of how downstream mixing occurs in a laminar hypersonic boundary layer. Further, these results could aid the validation process of numerical and analytical tools that aim to model various phenomena involving laminar mixing in high-speed flows.

Appendix 1: Calculation of flow quantities

In the Ludwig tube mode, pre-heated pressurised air is released into an evacuated test section by opening a plug valve. The air flows through a plenum and then is accelerated by a Laval nozzle before reaching the test section, where the flat-plate model is mounted. For the current experiments, a fill pressure of $p_{fill} = 2000$ kPa and a fill temperature of $T_{fill} = 500$ K are selected. The pressure in the plenum

upstream of the Laval nozzle is measured and approximated as the total pressure, p_0 . The total temperature, T_0 , is measured in the test section using differentially heated aspirated thermocouples as described in a previous work by Hermann et al. (2019a). When a shot is fired, the sudden opening of the plug valve releases expansion waves that travel upstream and reflect back downstream. Each of these reflected expansion waves causes a drop in p_0 and T_0 , resulting in a change of the flow condition as shown in Figs. 9 and 10. This feature of the tunnel enables testing at multiple quasi-steady conditions—each lasting for approximately 30 ms—from one single shot. These quasi-steady conditions are henceforth referred to as Conditions 1, 2, 3, 4, and 5 (annotated in Figs. 9 and 10). The Condition 0 is not considered as it is relatively unsteady.

Since $AoA = 0^\circ$, the edge Mach number, M_e , is equal to the free-stream Mach number, $M_\infty = 7$. The static edge pressure, p_e , is measured by the pressure transducers instrumented on the flat plate.

The edge velocity is calculated by the equation

$$u_e = M_e \sqrt{\gamma R T_e}, \tag{11}$$

where γ and R are, respectively, the isentropic exponent and specific gas constant of air. The edge unit Reynolds number is obtained from the equation

$$Re_u = \frac{\rho_e u_e}{\mu(T_e)}, \tag{12}$$

where $\mu(T_e)$ is the dynamic viscosity of the flow. Since $T_e < 89$ K, Keyes' viscosity model (Keyes 1952), given as

$$\mu(T_e) = \frac{1.488 \times 10^{-6} \sqrt{T_e}}{1 + \frac{122.1}{T_e} \times 10^{-\frac{5}{T_e}}}, \tag{13}$$

is employed. The obtained transient unit Reynolds number is plotted in Fig. 10.

The blowing ratio, i.e. the ratio of the injected coolant mass flux to the boundary-layer edge mass flux, is defined as

$$F = \frac{\rho_c u_c}{\rho_e u_e}, \tag{14}$$

where the subscript 'c' denotes coolant quantities at the surface. Due to continuity, the mass flux in the plenum and the mass flux injected into the boundary layer are equal; hence,

$$\rho_c u_c = \rho_{inj} u_{inj}, \tag{15}$$

where the subscript 'inj' stands for quantities inside the plenum. The density of the coolant can be obtained from the ideal gas law,

$$\rho_{inj} = \frac{p_{inj}}{R_c T_{inj}}, \tag{16}$$

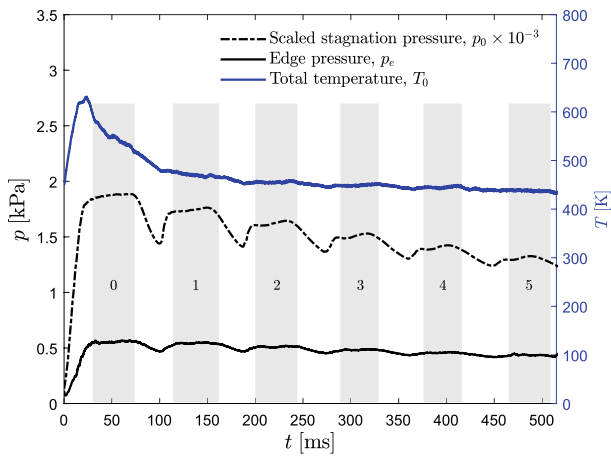


Fig. 9 Measured stagnation pressure, p_0 , edge pressure, p_e , and total temperature, T_0 , versus test time, t , from one single shot

where R_c is the specific gas constant of the coolant gas. Substituting Eqs. (12), (14), (15), (16), and $p_{out} = p_e$ in the integrated version of the Darcy–Forchheimer equation (Ifti et al. 2022) yields a form of the Darcy–Forchheimer equation that is directly dependent on the blowing ratio and unit Reynolds number given as follows:

$$\frac{p_{inj}^2 - p_e^2}{2LR_c T_{inj}} = \frac{Re_u \mu(T_e) \mu_c(T_{inj})}{K_D} F + \frac{(Re_u \mu(T_e))^2}{K_F} F^2. \quad (17)$$

The values of permeability coefficients, K_D and K_F , are given in Table 2 along with their uncertainties.

With a known unit Reynolds number, Re_u , and a plenum pressure, p_{inj} , the positive solution to Eq. (17) with respect to ‘ F ’ directly yields the blowing ratio. Note that the gas temperature, T_{inj} , measured by the thermocouple in the plenum

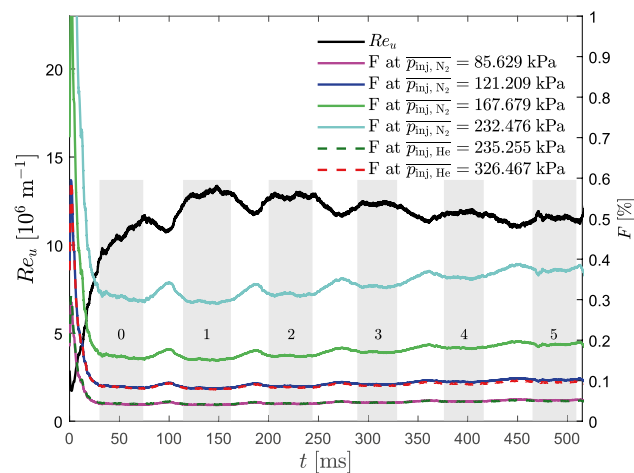


Fig. 10 Unit Reynolds number, Re_u , and blowing ratio, F , versus test time, t . The values of plenum pressure, p_{inj} , are averaged over the test time

is close to room temperature, and therefore, the coolant gas viscosity, $\mu_c(T_{inj})$, is calculated using Sutherland’s model (Sutherland 1853) with appropriate constants for the coolant gas in use. When HDT is fired, a constant gas pressure is set in the plenum by the gas injection system in the HDT. This plenum pressure, p_{inj} , is measured during each test by the pressure transducer fitted in the plenum. In Fig. 10, the transient blowing ratios obtained from Eq. (17) are illustrated for six different plenum pressures (Cases 1 to 6). Since the unit Reynolds number drops over time during the whole test period, the blowing ratio increases over time. Similar to the unit Reynolds number, the blowing ratio remains almost constant over each condition, from Condition 1 to Condition 5. As a result, five different blowing ratios are achieved from one single shot.

Appendix 2: Repeatability

Shot-to-shot repeatability in the final span-wise averaged concentration effectiveness is demonstrated in Fig. 11. Here, results from two shots, 1190 and 1199, independently calibrated by shots, 1191 and 1198, respectively, are plotted. The results are within $\eta_c = \pm 0.05$.

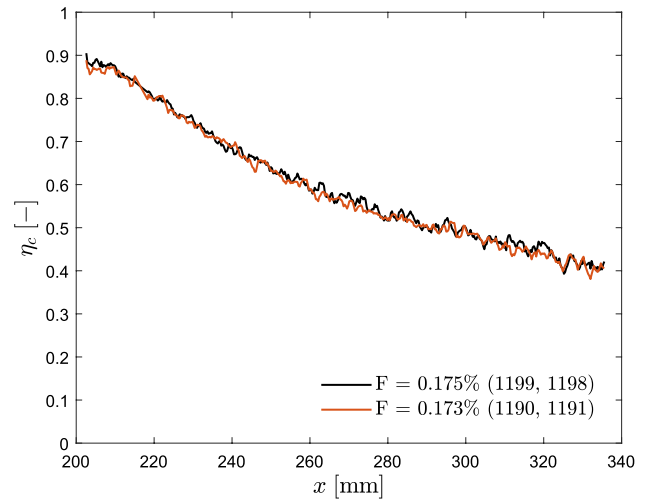


Fig. 11 Repeatability: span-wise averaged concentration effectiveness, η_c , versus stream-wise direction, x , for shot 1199 calibrated with shot 1198 (black) and shot 1190 calibrated with shot 1191 (red)

Appendix 3: Uncertainty analysis

The Kulites were calibrated against a reference pressure gauge (Infcon CDG025D) within the range of operation for the test campaign. The systematic uncertainties from installation effects for the Kulites and the reference

Table 2 Permeability coefficients and their corresponding uncertainties for UHTC-7 (Ifti et al. 2022)

Sample ID	K_D [10^{-14} m ²]	K_F [10^{-7} m]	L [mm]
UHTC-7	3.726 ± 0.061	1.97 ± 0.37	5

gauge are estimated to be $\pm 1\%$ and $\pm 0.5\%$, respectively. The reference gauges has a reading error of $\pm 0.2\%$. The final systematic uncertainty for the calibrated Kulites are $\sqrt{1^2 + 0.5^2 + 0.2^2} = 1.14\%$, which represents the uncertainties in the measured static pressure, p_e , and the plenum pressure, p_{inj} . The uncertainty in the total temperature, T_0 , and hence the edge temperature, T_e , is estimated to be ± 3 K assuming steady state (Hermann et al. 2019a). Error propagation according to Moffat (1988) yields uncertainties of $\pm 3.34\%$ and $\pm 9.95\%$ for the edge velocity, u_e , and edge density ρ_e , respectively. An uncertainty of $\pm 11.0\%$ in F is obtained by an error propagation in Eq. (17) with the uncertainties in p_e , p_{inj} , T_e , u_e , ρ_e , K_D and K_F (see Table 2) as input sources.

With an estimated uncertainty of $\pm 9.5\%$ in the wall heat flux, \dot{q}_w (Hermann et al. 2019a), a further error propagation yields uncertainties of $\pm 25.6\%$ for the Stanton number, St , and $\pm 29.5\%$ for the blowing parameter, B_h .

As reported in Ewenz Rocher et al. (2022), the overall uncertainty in the PSP intensity ratio, I_{ref}/I , is $\leq 2\%$. Since it is calibrated with pressure data obtained from the Kulites, the final error in the pressure measurements from PSP is $\leq \sqrt{2^2 + 1.14^2} = \pm 2.3\%$. According to Eq. (4), this results in an uncertainty of $\leq \pm 5\%$ in η_c .

The flat-plate model was mounted on a custom-made table in the test section, which has been used in several campaigns before Hermann et al. (2018); Ewenz Rocher et al. (2022) for an angle of attack of $AoA = 0^\circ$. Its relative positioning with respect to the tunnel is consistent with the automated traverse employed in Wylie (2020). The incoming flow can be misaligned with respect to the model by up to -0.4° (Wylie 2020, Chapter 5). A conservative estimate of $\pm 0.4^\circ$ of uncertainty in the angle of attack results in uncertainties of up to 7.1% and 2.0% in the edge pressure, p_e , and the edge temperature, T_e , respectively.

Appendix 4: Mach angle analysis

Results of a Mach angle analysis for the flat-plate model at Mach 7 are shown in Fig. 12. The Mach cones emanating from the two corners meet at a distance of $x = 433$ mm from the leading edge. The green zone between the two cones is free of disturbance stemming from the corners, and therefore, a 2D flow can be assumed here.

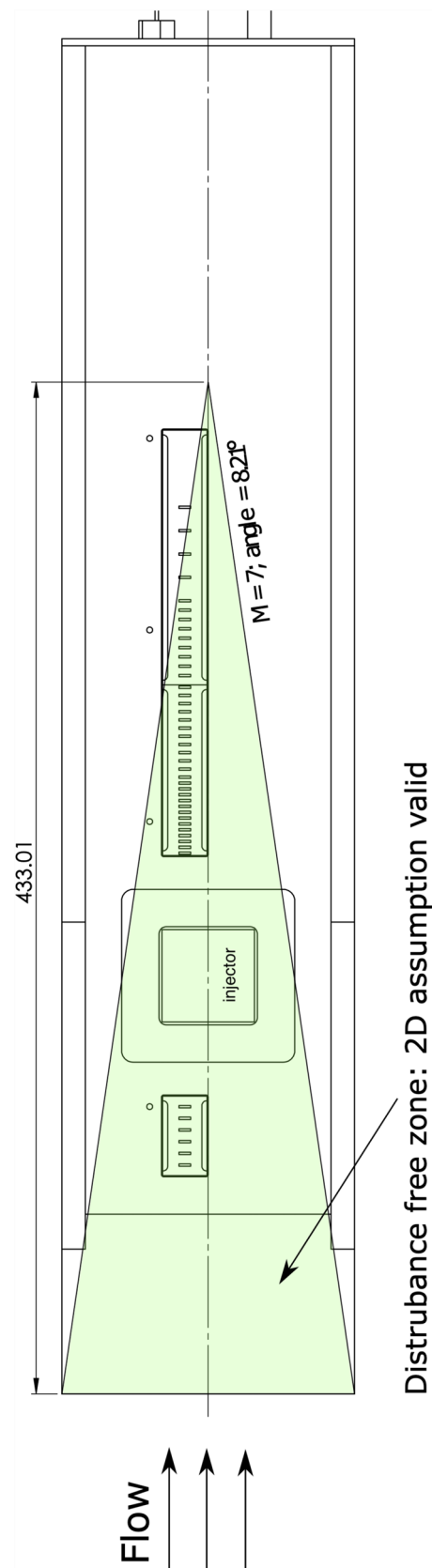


Fig. 12 Schematic of the flat-plate model with Mach cones emanating from the corners. The green zone denotes the area where a 2D assumption is valid

Acknowledgements The funding for this research by the EPSRC grant ‘Transpiration Cooling Systems for Jet Engine Turbines and Hypersonic Flight’ (reference: EP/P000878/1) is gratefully acknowledged. The authors would like to thank Gregory King for his help with the instrumentation of the experimental model; Maïlys Buquet for operating the tunnel; Dr Markus Kloker and Dr Adriano Cerminara for their discussions; and Dr Ikhyun Kim for his support during the experimental campaign.

Open Access This article is licensed under a Creative Commons Attribution 4.0 International License, which permits use, sharing, adaptation, distribution and reproduction in any medium or format, as long as you give appropriate credit to the original author(s) and the source, provide a link to the Creative Commons licence, and indicate if changes were made. The images or other third party material in this article are included in the article's Creative Commons licence, unless indicated otherwise in a credit line to the material. If material is not included in the article's Creative Commons licence and your intended use is not permitted by statutory regulation or exceeds the permitted use, you will need to obtain permission directly from the copyright holder. To view a copy of this licence, visit <http://creativecommons.org/licenses/by/4.0/>.

References

- Eckert ERG (1956) Engineering relations for heat transfer and friction in high-velocity laminar and turbulent boundary-layer flow over surfaces with constant pressure and temperature. *Trans Am Soc Mech Eng* 78(6):1273
- Ewenz Rocher M, Hermann T, McGilvray M, Ifti HS, Vieira J, Hambidge C, Quinn MK, Grossman M, Vandeperre L (2022) Pressure-sensitive paint diagnostic to measure species concentration on transpiration-cooled walls. *Exp Fluids* 63(1):1–11. <https://doi.org/10.1007/s00348-021-03355-9>
- Fujiwara K, Sriram R, Kontis K, Ideta T (2017) Review on film cooling in high-speed flows. In: 31st international symposium on shock waves 2. Springer, Cham, pp 939–946. https://doi.org/10.1007/978-3-319-91017-8_118
- Goldstein RJ (1971) Film Cooling. *Adv Heat Trans* 7:321–379. [https://doi.org/10.1016/S0065-2717\(08\)70020-0](https://doi.org/10.1016/S0065-2717(08)70020-0)
- Gülhan A, Braun S (2010) An experimental study on the efficiency of transpiration cooling in laminar and turbulent hypersonic flows. *Exp Fluids* 50(3):509–525. <https://doi.org/10.1007/s00348-010-0945-6>
- Haven BA, Kurosaka M (1997) Kidney and anti-kidney vortices in crossflow jets. *J Fluid Mech* 352:27–64. <https://doi.org/10.1017/S0022112097007271>
- Hermann T, Ifti HS, McGilvray M, Doherty L, Geraets RP (2018) Mixing characteristics in a hypersonic flow around a transpiration cooled flat plate model. In: International conference on high-speed vehicle science and technology (HiSST), Moscow, Russia
- Hermann T, McGilvray M, Hambidge C, Doherty L, Buttsworth D (2019a) Total temperature measurements in the oxford high density tunnel. In: International conference on flight vehicles, aerothermodynamics and re-entry missions and engineering, FAR, Monopoli, Italy
- Hermann T, McGilvray M, Naved I (2019) Performance of transpiration-cooled heat shields for reentry vehicles. *AIAA J* 10(2514/1):J058515
- Heufer KA, Olivier H (2008) Experimental and numerical study of cooling gas injection in laminar supersonic flow. *AIAA J* 10(2514/1):34218
- Heufer KA, Olivier H (2008b) Experimental study of active cooling in 8 laminar hypersonic flows. In: RESPACE—key technologies for reusable space systems, Springer, Berlin, pp 132–150. https://doi.org/10.1007/978-3-540-77819-6_8
- Hombsch M, Olivier H (2013) Film cooling in laminar and turbulent supersonic flows. *J Spacecr Rocket* 10(2514/1):A32346
- Ifti HS, Hermann T, McGilvray M (2019) Transpiration cooling at mach 5 employing porous UHTC. In: Conference on flight vehicles, aerothermodynamics and re-entry missions and engineering (FAR), European Space Agency, Monopoli, Italy
- Ifti HS, Hermann T, McGilvray M, Larrimbe L, Hedgecock R, Vandeperre L (2022) Flow characterization of porous ultra-high-temperature ceramics for transpiration cooling. *AIAA J* 10(2514/1):J061009
- Kays WM, Crawford ME, Weigand B (2005) Convective heat and mass transfer, 4th edn. McGraw-Hill Higher Education
- Keller MA, Kloker MJ, Olivier H (2015) Influence of cooling-gas properties on film-cooling effectiveness in supersonic flow. *J Spacecr Rocket* 10(2514/1):A33203
- Keyes FG (1952) The heat conductivity, viscosity, specific heat and Prandtl numbers for thirteen gases
- McGilvray M, Doherty LJ, Neely AJ, Pearce R, Ireland P (2015) The Oxford high density tunnel. In: 20th AIAA international space planes and hypersonic systems and technologies conference, American Institute of Aeronautics and Astronautics, Reston, Virginia, p 17. <https://doi.org/10.2514/6.2015-3548>
- Moffat RJ (1988) Describing the uncertainties in experimental results. *Exp Thermal Fluid Sci* 1(1):3–17. [https://doi.org/10.1016/0894-1777\(88\)90043-X](https://doi.org/10.1016/0894-1777(88)90043-X)
- Murray AV, Ireland P, Wong TH, Tang SW, Rawlinson AJ (2017) High resolution experimental and computational methods for modelling multiple row effusion cooling performance. In: Proceedings of European conference on turbomachinery fluid dynamics thermodynamics ETC, April; Stockholm, Sweden
- Oldfield MLG (2008) Impulse response processing of transient heat transfer gauge signals. *J Turbomach* 130(2):709. <https://doi.org/10.1115/1.2752188>
- Quinn MK, Yang L, Kontis K (2011) Pressure-sensitive paint: effect of substrate. *Sensors* 11(12):11649–11663. <https://doi.org/10.3390/s111211649>
- Richards BE, Stollery JL (1979) Laminar film cooling experiments in hypersonic flow. *J Aircr* 10(2514/3):58502
- Schultz DL, Jones TV (1973) Heat-transfer measurements in short-duration hypersonic facilities. Tech. Rep. AD-758 590, Advisory Group For Aerospace Research and Development, North Atlantic Treaty Organization
- Sellers M, Nelson M, Crafton JW (2016) Dynamic pressure-sensitive paint demonstration in AEDC propulsion wind tunnel 16T. In: 54th AIAA aerospace sciences meeting, San Diego, California, USA. <https://doi.org/10.2514/6.2016-1146>
- Sutherland W (1853) LII. The viscosity of gases and molecular force. *J Sci* 36(223):507–531. <https://doi.org/10.1080/14786449308620508>
- Tanno H, Komuro T, Itoh K, Kuhn M, Petkov I, Esser B (2016) Transpiration cooling experiments in free-piston shock tunnel HIEST. In: Eighth European workshop on thermal protection systems and hot structures, Noordwijk, Netherlands
- van Driest ER (1956) The problem of aerodynamic heating. *Aeronaut Eng Rev* 15(10):26–41
- Wylie S (2020) Hypersonic boundary layer instability measurements at low and high angles of attack. PhD thesis, University of Oxford
- Wylie S, McGilvray M (2019) HIFiRE-1 post-flight experiments in the University of Oxford’s high density tunnel. In: AIAA Scitech 2019 forum, San Diego, California. <https://doi.org/10.2514/6.2019-1940>

Publisher's Note Springer Nature remains neutral with regard to jurisdictional claims in published maps and institutional affiliations.